Analytical expression for the electronic stopping cross section of atomic gas targets for hydrogen projectiles

R. Cabrera-Trujillo ●*

*Instituto de Ciencias Físicas, Universidad Nacional Autónoma de México, Avenida Universidad S/N, Cuernavaca, Morelos 62251, Mexico
and Theoretische Chemie, Physikalisch-Chemisches Institut, Universität Heidelberg, INF 229, 69120 Heidelberg, Germany*

The energy deposition of hydrogen projectiles in material targets is of great importance in material damage, as well as in radiotherapy and dosimetry, particularly for the treatment of cancer tumors. The energy-loss description has to take into account electronic excitation, electron transfer, and nuclear displacement for collisions with atomic targets. Each of these processes become relevant at different projectile collision energies, making the modeling of the full energy-loss curve difficult to accomplish. In this article, an analytical expression for the electronic stopping cross section of atomic gas targets at nonrelativistic velocities for hydrogen ions is reported. As the energy deposition process requires a correct description of the energy-loss and scattering process, our formulation uses theoretical results at low collision energies derived from *ab initio* electron-nuclear dynamics (END), which accounts for the nuclear displacement, electronic excitation, and charge-transfer process. At high collision energies, the expression is based on the independent particle orbital description [R. Cabrera-Trujillo, Phys. Rev. A **60**, 3044 (1999)] combined with Bethe's analytical expression obtained through a harmonic oscillator representation of a target [L. Trujillo-Lopez *et al.*, Radiat. Phys. Chem. **156**, 150 (2019)]. The two approaches are matched at intermediate energies through the charge-exchange cross sections obtained from the END approach in a probabilistic interpretation of the processes [E. Montenegro *et al.* Phys. Lett. A **92**, 195 (1982)]. The excellent agreement obtained when compared to experimental data for H to Ar gas targets ($Z \leqslant 18$) when hydrogen projectiles impinge gives support to the theoretical arguments implied in its derivation. The analytical expression is simple and has the correct asymptotic behavior at low and high collision energies. Furthermore, the formula explains properly the threshold effects at low collision energies which are the result of polarization effects and energy gaps in the excitation process of the target, as confirmed by our *ab initio* results.

I. INTRODUCTION

The study of the penetration of charged particles through matter has been the subject of continuous theoretical and experimental efforts since the pioneering work of Rutherford, which gave rise to our understanding of quantum mechanics [1]. However, the many-body character of atomic and molecular systems imposes serious difficulties to fully understand the various mechanisms that participate in the slowing down process of projectiles. The electronic stopping cross section is a response of the system electrons to the energy deposited by the projectile; electrons are promoted to excited states [2]. The electronic excitations are classified as ionization [3,4], charge transfer [5], excitation [6], and molecular fragmentation (bond breaking) [7]. Thus, the electronic stopping curve shows three separate regimes, which are a consequence of the different processes that participate in the energy-loss phenomenon more or less dominantly, according to their probability to occur. At high energies, the ionization of individual atoms becomes the main source of energy loss. As the projectile slows down, other processes such as electron capture and loss and excitations become impor-

tant. At low velocities, a "friction" mechanism becomes increasingly important, leading, in principle, to a velocity-proportional behavior. The first theoretical studies of the electronic stopping cross section were carried out by Bohr [8,9] and Bethe [3,4] at high collision energies. In the low collision energy region several theoretical approaches have been proposed [10–12]. One of these approaches is due to Lindhard, which evaluates the interaction of a moving charge through a uniform free-electron gas via a complex dielectric response function which accounts for the polarization effects of the target electronic cloud. Another approach is Firsov's model [12], which describes the projectile and target as Thomas-Fermi atoms whose electrons exchange momentum, consequently producing a net "drag force" on the projectile, resulting, theoretically, in a linear velocity dependence of the electronic stopping cross section. However, there is not a theory that accounts for all these processes for the whole energy range of the projectile.

There have been many efforts to formulate empirical or semiempirical approaches to generate an equation valid for all velocities and ion-target combinations. Burenkov *et al.* [13] developed a semiclassical theory to account for the inelastic energy loss of heavy ions, valid for a wide range of energies. Sugiyama [14] proposed a composite formula for the electronic stopping valid in the intermediate-energy range.

---

*trujillo@icf.unam.mx

Montenegro, Cruz, and Vargas (MCV) [15] proposed a universal formula for the electronic stopping cross section without adjustable parameters that connects the linear behavior at low collision energies with the Bethe region at high collision energies. Later, Wang and He proposed a modification to the MCV equation for highly charged projectiles [16]. Kobadayi and Gümüs [17] and Gümüs and Kobadayi [18] have made comparisons of electronic stopping cross sections and ion ranges for heavy ions incident in Si and SiO$_2$ with formulas based on the MCV universal proposal with excellent comparison to the experiment. The MCV formula uses a linear velocity dependence expression for the low-energy collision region, as deduced by Ahkiezer and Davydov [19] with parameters being tabulated by Andersen and Ziegler [20].

From the computational point of view, there is the SRIM (stopping and ranges of ions in matter) computer program that calculates the electronic and nuclear energy loss of ions in matter [21] of any ion in any material based on an averaged parametrization of a vast range of experimental data [20] through a universal interaction potential. Another approach to study the stopping cross section at intermediate energies is due to Schiwietz [22]. The Schiwietz approach is based on the coupled-channel approach to solve the time-dependent Schrödinger equation for a target with an active electron with the nuclear motion being described approximately by Newton's equations of motion in a classical-trajectory Monte Carlo approach. A new promising first-principles approach that has been used to study the electronic stopping cross section is due to Artacho [23,24]. The approach uses the time-dependent density-functional theory (TDDFT) where adiabatic forces acting on nuclei are calculated to perform molecular dynamics calculations, which follow the Newtonian dynamics of classically treated nuclei. However, an *ab initio* description of the energy deposition at low collision energies that accounts for electronic excitations, charge transfer, and nuclei coupling has not been possible. Furthermore, there is experimental evidence that at low collision velocities, the theoretical description for the electronic stopping cross section fails to properly describe the energy-loss process [25,26] due to threshold effects.

In this article, we propose an analytical general expression for the electronic stopping cross section of hydrogen projectiles valid for nonrelativistic collision energies, in all gas targets. We present results for hydrogen beams colliding on all atomic targets with $Z_t \leqslant 18$. At low collision energies, excitations and charge exchange are accounted for by the first-principles *ab initio* electron-nuclear dynamics (END) approach [27] to properly describe the energy-loss process, differential scattering, charge transfer, and target excitations of the involved atoms. At high collision energies a simple universal formula, already reported by the author [28], has been matched to the low END energy results following a similar procedure as that of MCV [15].

II. THEORETICAL APPROACH

In order to set the basis of our theoretical formulation, let us start reviewing the concept of energy loss and stopping cross section. Let us consider a target material of thickness Δx and n_2 atoms per volume (target number density). For

a projectile impinging in this material, the energy loss is given by $\Delta \mathcal{E} = \sum_i \omega_i \Delta E_i$, where ω_i is the probability for the projectile to have an energy loss ΔE_i at the ith collision when the target and the sum is over all the collision events occurring in the path. The collision probability is given by $\omega_i = n_2 \sigma_i \Delta x$, where σ_i is the cross section for the projectile to have the ith collision with a target. Consequently, the projectile energy loss is $\Delta \mathcal{E} = n_2 \Delta x \sum_i \sigma_i \Delta E_i$. In the limit of infinitesimal thickness, one defines the stopping cross section as

$$\frac{1}{n_2} \frac{d\mathcal{E}}{dx} = S = \int \Delta E \, d\sigma. \tag{1}$$

This definition of the stopping cross section, i.e., the energy loss of a projectile per path traveled and per target, can be expressed as

$$S(E_p) = \int \Delta E(E_p) \frac{d\sigma(E_p)}{d\Omega} d\Omega, \tag{2}$$

where $d\sigma/d\Omega$ is the differential cross section for the projectile to be scattered within a solid angle $d\Omega$. Here, E_p is the projectile initial kinetic energy. Therefore, one observes that the stopping cross section per target depends directly on how much energy the projectile loses, ΔE, and how the scattering process occurs through the differential cross section $d\sigma/d\Omega$. For the particular case of a classical description of the scattering process, the classical differential cross section is given by

$$\frac{d\sigma}{d\Omega} = \frac{b}{\sin \theta} \left| \frac{db}{d\theta} \right|, \tag{3}$$

where $d\Omega = \sin \theta d\theta d\varphi$ is the differential of a solid angle and the impact parameter b is related to the angular momentum of the scattering process. With this, the stopping cross section can be recast as

$$S(E_p) = 2\pi \int b \Delta E \, db. \tag{4}$$

Furthermore, the classical differential cross section can be improved by incorporating semiclassical corrections due to quantum effects on the projectile trajectory. The author has already achieved this through the Schiff approximation [29,30], where the differential cross section is given by

$$\frac{d\sigma}{d\Omega} = \frac{k_f}{k_i} |f(\theta, \varphi)|^2, \tag{5}$$

with

$$f(\theta, \varphi) = ik_i \int_0^\infty J_0(qb)(e^{2i\delta(b)} - 1) b \, db \tag{6}$$

being the scattering amplitude [30]. Here, $J_0(x)$ is the Bessel function of zero order, $\hbar q = \hbar |\mathbf{k}_f - \mathbf{k}_i|$ is the momentum transfer, which depends on the scattering angle θ, and $\delta(b)$ is the semiclassical phase shift given by

$$\Theta(b) = \frac{1}{2k_i} \frac{d\delta(b)}{db}, \tag{7}$$

where $\Theta(b) = \theta$ is the deflection function for the scattering process which describes the attractive and repulsive behaviors of the projectile-target interaction [30]

Thus, a proper description of the energy-loss process as well as of the scattering process is required in order to obtain a reliable stopping cross-section description.

A. Electron-nuclear dynamics

In order to account for the electron-capture, electronic excitations, and energy-loss processes, we use a nonadiabatic approach that takes into account the electronic and nuclear coupling within the time-dependent variational principle (TDVP). This method is called electron-nuclear dynamics (END) and has the advantage that it is not restricted to straight-line trajectories. As the details of the END method have been reported elsewhere [27,31], we present here only a brief summary of the theory.

The END wave function is expressed as

$$|\psi\rangle = |z, \mathbf{R}, \mathbf{P}\rangle|\mathbf{R}, \mathbf{P}\rangle = |z\rangle|\phi\rangle, \tag{8}$$

where $|\phi\rangle = |\mathbf{R}, \mathbf{P}\rangle$ is the nuclear wave function and $|z, \mathbf{R}, \mathbf{P}\rangle$ is the electronic wave function. Here, R and P are $3N$-dimensional arrays of the positions and momenta of all nuclei and z are the probability amplitudes for the excitations.

The nuclear wave function $|\phi\rangle$ is described by a Gaussian wave packet

$$|\phi\rangle = \prod_l \exp\left[-\frac{1}{2}\left(\frac{\mathbf{X}_l - \mathbf{R}_l}{\beta_l}\right)^2 + i\mathbf{P}_l \cdot (\mathbf{X}_l - \mathbf{R}_l)\right], \tag{9}$$

where $\mathbf{R}_l$ and $\mathbf{P}_l$ are the average position and momentum of the lth nucleus. The width parameters β_l are taken to the narrow wave-packet limit ($\beta_l \to 0$, for all β_l).

The electronic wave function is expressed as a complex, spin-unrestricted single determinant,

$$|z\rangle = \det\{\chi_i(\mathbf{x}_j)\}. \tag{10}$$

Here, $\mathbf{x}_j$ is the three-dimensional coordinate of electron j. The determinantal wave function is built from nonorthogonal dynamical spin orbitals

$$\chi_i = \phi_i + \sum_{j=N+1}^{K} z_{ij}\phi_j, \quad i = 1, 2, \ldots, N, \tag{11}$$

which in turn are expressed in terms of a basis of atomic spin orbitals ϕ_i of rank K. Here, z_{ij} are the amplitude probabilities for excitations. The spin orbitals are formed from a Gaussian basis set centered on the average positions $\mathbf{R}_l$ of the participating atomic nuclei, which take into account the momentum of the electron explicitly through electron translation factors (ETFs). The particular form of parametrization of $|z\rangle$ with complex, time-dependent coefficients z_{ij} is due to Thouless [32], and is an example of a so-called generalized coherent state [33].

Application of the TDVP produces a set of dynamical equations that govern the time evolution of the dynamical variables $\{z, \mathbf{R}, \mathbf{P}\}$. The END dynamical equations are expressed in matrix form as [27]

$$\begin{pmatrix} \mathbf{0} & -i\mathbf{C}^* & -i\mathbf{C}_\mathbf{R}^* & \mathbf{0} \\ i\mathbf{C} & \mathbf{0} & i\mathbf{C}_\mathbf{R} & -i\mathbf{C}_\mathbf{P} \\ i\mathbf{C}_\mathbf{R}^\dagger & -i\mathbf{C}_\mathbf{R}^\mathbf{T} & \mathbf{C}_{\mathbf{RR}} & -\mathbf{I} + \mathbf{C}_{\mathbf{RP}} \\ i\mathbf{C}_\mathbf{P}^\dagger & -i\mathbf{C}_\mathbf{P}^\mathbf{T} & \mathbf{I} + \mathbf{C}_{\mathbf{RP}} & \mathbf{C}_{\mathbf{PP}} \end{pmatrix} \begin{pmatrix} \dot{\mathbf{z}} \\ \dot{\mathbf{z}}^* \\ \dot{\mathbf{R}} \\ \dot{\mathbf{P}} \end{pmatrix} = \begin{pmatrix} \nabla_\mathbf{z} E \\ \nabla_{\mathbf{z}^*} E \\ \nabla_\mathbf{R} E \\ \nabla_\mathbf{P} E \end{pmatrix}, \tag{12}$$

where $\nabla_\mathbf{y} E = \partial E/\partial \mathbf{y}$ is the gradient (force) on the energy by the variable $\mathbf{y}$ and E is the total energy of the system given by

$$E = \sum_k \frac{P_k^2}{2M_k} + \frac{\langle z, \mathbf{R}, \mathbf{P}|H_{\text{el}}|z, \mathbf{R}, \mathbf{P}\rangle}{\langle z, \mathbf{R}, \mathbf{P}|z, \mathbf{R}, \mathbf{P}\rangle}. \tag{13}$$

Here, H_{el} is the electronic Hamiltonian and contains the nuclear-nuclear repulsion potential energy. The nonadiabatic coupling terms between the electronic and nuclear dynamics are expressed in terms of the elements of the dynamical metric on the left. In particular,

$$C = \left.\frac{\partial^2 \ln S(z^*, \mathbf{R}, \mathbf{P}, z, \mathbf{R}', \mathbf{P}')}{\partial z^* \partial z}\right|_{\mathbf{R}'=\mathbf{R},\mathbf{P}=\mathbf{P}'}, \tag{14}$$

$$C_R = \left.\frac{\partial^2 \ln S(z^*, \mathbf{R}, \mathbf{P}, z, \mathbf{R}', \mathbf{P}')}{\partial z^* \partial \mathbf{R}'}\right|_{\mathbf{R}'=\mathbf{R},\mathbf{P}=\mathbf{P}'}, \tag{15}$$

$$C_{RR} = -2\,\text{Im}\left.\frac{\partial^2 \ln S(z^*, \mathbf{R}, \mathbf{P}, z, \mathbf{R}', \mathbf{P}')}{\partial \mathbf{R} \partial \mathbf{R}'}\right|_{\mathbf{R}'=\mathbf{R},\mathbf{P}=\mathbf{P}'}, \tag{16}$$

with similar definitions for C_{RP}, C_P, and C_{PP}. These coupling terms are defined in terms of the overlap $S(z^*, \mathbf{R}, \mathbf{P}, z, \mathbf{R}', \mathbf{P}') = \langle z, \mathbf{R}', \mathbf{P}'|z, \mathbf{R}, \mathbf{P}\rangle$ of the determinantal states of two different nuclear configurations. When the effects of the electron translation factors are neglected, these sets of equations reduce to a simple form [34] with the purely classical equation of motion for the nuclear position.

In contrast to other approaches used to study energy deposition, e.g., Schiwietz [22] or Artacho [23,24], END uses trajectories as given by the dynamical system in a nonadiabatic approach and all degrees of freedom are included. The only exception is ionization due to the lack of continuum wave functions in a Gaussian basis set.

Analysis of the collision requires the specification of initial conditions of the system under consideration. The initial projectile velocity is set parallel to the z axis and directed towards the stationary target with an impact parameter b along the xy plane. The target atom has been initially placed at the origin of a Cartesian laboratory coordinate system. In these calculations the projectile is initially set at a distance of 20 a.u. from the target and in the self-consistent electronic ground state. The impact parameter b is chosen in the range 0–20 a.u. in steps of 0.1 from 0.0 to 4.0, in steps of 0.2 from 4.0 to 6.0, in steps of 0.4 from 6 to 10, and in steps of 1.0 from 10 to 20 a.u. This gives a total of 70 fully dynamical trajectories for each projectile energy.

The electronic basis set used for the atoms from $1 \leqslant Z_p \leqslant 18$ is the augmented correlation-consistent polarized valence double zeta (aug-cc-pVDZ) basis set of Dunning [35] consisting of $[5s3p/2s2p]$ orbitals for $1 \leqslant Z_t \leqslant 10$ and $[13s9p2d/5s4p2d]$ for $11 \leqslant Z_t \leqslant 18$. These basis sets provide a good compromise between computational time and a proper description of the low excited states of the system. For instance, a calculation at 10 eV/amu for hydrogen targets would take around 2 h in a 3.2-GHz computer, while at 5 keV/amu it takes a few minutes per impact parameter. However, for Ar at 10 eV it would take 20 days at 10 eV and for 5 keV/amu around 15 h for these basis sets. As this approach lacks the proper description of the continuum states, ionization processes are not properly described. Thus, we

cannot apply the END approach to high collision energies yet, so consequently we limit the applicability of END to collision energies below 5 keV/amu (0.4475 a.u. in Bohr velocity) to account for the low excitation spectrum.

1. Stopping cross section

Once the wave function is determined at the end of the time evolution, the electron-capture or electron-loss probability, as a function of the impact parameter b, is obtained by a projection of the projectile nth state as

$$P_n(b, E_p) = |\langle \psi_n | \Phi(b, E_p) \rangle|^2, \tag{17}$$

where ψ_n is the final capture state of the projectile and Φ is the final evolved molecular wave function. The total electron-capture probability $P(b)$ is the sum over all the state contributions.

The charge-exchange cross section is given by

$$\sigma(E_p) = 2\pi \int b P(b, E_p) db. \tag{18}$$

Here, P denotes either the total or the nth state electron-capture probability.

The END approach provides the final momentum of the nuclei, which allows one to determine the kinetic energy loss for the projectile as $\Delta E(b, E_p) = E_p^f(b, E_p) - E_p$, where E_p^f is the projectile final kinetic energy and E_p the projectile initial kinetic energy. From energy conservation, we have that

$$-\left(E_p^f - E_p\right) = \left(E_{p,e}^f - E_{p,e}^i\right) + \left(E_{t,e}^f - E_{t,e}^i\right)$$
$$+ \left(E_t^f - E_t^i\right) \equiv -\Delta E, \tag{19}$$

where the superscripts i or f stand for initial or final, while the subscripts p or t stand for projectile or target. Here, the subindex e indicates the electronic energy in the projectile or target. This means that for a projectile energy loss $\Delta E < 0$, there is an energy gain in the target nuclear energy and in the excitation energy of the system. Thus, the stopping cross section, that is, the cross section for the projectile kinetic energy loss, is given by

$$S(E_p) = -2\pi \int_0^\infty b \, \Delta E(b, E_p) db. \tag{20}$$

This is a measure of the nonadiabatic effects that take place during the collision as the projectile kinetic energy is modified by the momentum and charge transferred during the collision. The negative sign is to assure that S is positive for energy loss [36]. With this, the electronic stopping cross section is given as

$$S_e(E_p) = 2\pi \int_0^\infty b \, \Delta E_e(b, E_p) db, \tag{21}$$

and the nuclear stopping cross section as

$$S_n(E_p) = 2\pi \int_0^\infty b \, \Delta E_n(b, E_p) db. \tag{22}$$

Here, $\Delta E_e = (E_{p,e}^f - E_{p,e}^i) + (E_{t,e}^f - E_{t,e}^i)$ is the energy loss of the projectile that goes into electronic excitations and ionization in the projectile-target system and $\Delta E_n = (E_t^f - E_t^i)$ is the target recoil kinetic energy (nuclear displacement). These are positive quantities when the transferred energy is gained by the target through target excitations and target nuclei recoil. This approach has been used with success to describe the charge-exchange process in highly charged systems [37] as well as in the description of the electronic stopping cross section [38].

2. Projectile beam charge fraction

During the collision the beam has a fraction of charged components. Following the charge-state approach devised by Dalgarno and Griffing [39], the fractions of proton and hydrogen atoms in the beam are given by

$$f_{01} = \frac{\sigma_{01}}{\sigma_{01} + \sigma_{10}} = f(\text{H}^+) \tag{23}$$

and

$$f_{10} = \frac{\sigma_{10}}{\sigma_{01} + \sigma_{10}} = f(\text{H}), \tag{24}$$

where f_{ij} is the charge fraction for the projectile to go from an initial charge state i to a final charge state j, with the same meaning for the cross section σ_{if} (charge-transfer cross section). Note that we have neglected the formation of negative hydrogen during the collision [39]. Consequently, the stopping cross section is given by

$$S_e(v) = f(\text{H}) S_e(\text{H}) + f(\text{H}^+) S_e(\text{H}^+), \tag{25}$$

where $S_e(\text{H}^+)$ is the electronic stopping cross section when an initial proton projectile collides with a target and $S_e(\text{H})$ is the electronic stopping cross section for an initial neutral hydrogen projectile. Here, v is the initial projectile velocity, commensurate with the projectile initial kinetic energy E_p, i.e., $E_p = M_p v^2 / 2$, where M_p is the projectile mass.

A similar expression is used to obtain the nuclear stopping cross section

$$S_n(v) = f(\text{H}) S_n(\text{H}) + f(\text{H}^+) S_n(\text{H}^+), \tag{26}$$

which represents the averaged nuclear stopping cross section over the hydrogen beam charge fraction.

3. Low-energy threshold effects

For a binary collision, the minimum momentum transferred during a collision in the relative frame, obtained through energy conservation, is given by [38,40]

$$q_{\min} = \frac{\mu v}{\hbar} \left[1 - \sqrt{1 - \frac{2(E_n - E_0)}{\mu v^2}} \right], \tag{27}$$

where μ is the reduced mass of the projectile-target system, v the projectile incoming speed, and $E_n - E_0$ the electronic energy absorbed by the target from the initial state E_0 to the final state E_n. In order that the momentum transfer be enough for an electronic transition, it is necessary that the minimum momentum absorbed overcomes the electronic transition energy

$$\frac{\hbar^2 q_{\min}^2}{2m_e} \geqslant E_n - E_0. \tag{28}$$

Solving for the projectile energy for a target at rest, we obtain

$$E_p \geqslant \frac{\mu^2}{4M_p m_e}(E_n - E_0)\left[1 + \frac{m_e}{M_p}\right]^2, \tag{29}$$

where M_p is the projectile mass. This expression shows the discretized behavior of energy transfer and provides the theoretical explanation of a threshold energy for the first electronic excitation in the target. If we would have a continuum distribution of transition energies starting from zero, as is assumed in the atomic Thomas-Fermi model, the projectile would transfer energy continuously to the target for all projectile energies. However, this is not the case, and consequently electronic excitations demand a threshold velocity for the projectile in the electronic stopping cross section [38].

4. Analytic expression for S_e at low velocities

As mentioned before, in the low-energy region, the theory suggests a linear velocity dependence of the electronic stopping cross section. However, because of the discrete excitation spectrum of atoms and molecules, a threshold velocity appears depending on the density of the excitation spectrum, such that the electronic stopping cross section shows a bilinear velocity dependence. Our END results precisely show that behavior (see below). In order to properly describe it, we propose the following formula valid at low collision velocities,

$$S_e^L(v) = \begin{cases} Av, & v < v_{\text{tr}}, \\ Bv + C, & v > v_{\text{tr}}, \end{cases} \tag{30}$$

where A and B are the slopes of the electronic stopping cross section at low collision energy. Here, v_{tr} is the threshold velocity for the change of that behavior. Notice that by energy conservation assumptions, $S_e(v = 0) = 0$.

In order to obtain an analytical continuum expression, one proceeds as follows: Let us take the derivative of the previous equation,

$$\frac{dS_e^L(v)}{dv} = \begin{cases} A, & v < v_{\text{tr}}, \\ B, & v > v_{\text{tr}}, \end{cases}$$
$$= A + (B - A)\Theta(v - v_{\text{tr}}), \tag{31}$$

where $\Theta(x)$ is the Heaviside function, i.e., $\Theta(x) = 0$ if $x < 0$ and $\Theta(x) = 1$ if $x > 0$. In order to account for a smooth transition at $v = v_{\text{tr}}$, we replace the Heaviside function by an equivalent smooth function. In this case, we propose the Wood-Saxon function [41],

$$\Theta(x) \rightarrow \frac{1}{1 + e^{-x/\delta}}, \tag{32}$$

where δ is the diffuseness of the transition in the step of the Heaviside function. Consequently,

$$\frac{dS_e^L(v)}{dv} = A + \frac{(B - A)}{1 + e^{-(v - v_{\text{tr}})/\delta}}. \tag{33}$$

Integrating back again, we have that in the low-energy region

$$S_e^L(v) = C + Av + (B - A)\ln[1 + e^{(v - v_{\text{tr}})/\delta}]\delta, \tag{34}$$

with C an integration constant.

Using the fact that $S_e(v = 0) = 0$, we obtain

$$S_e^L(v) = Av + (B - A)\delta \ln\left[\frac{1 + e^{(v - v_{\text{tr}})/\delta}}{1 + e^{-v_{\text{tr}}/\delta}}\right]. \tag{35}$$

Mathematically, this expression is called a wedge function since it provides a mathematical expression for a wedge with a sharp edge. The sharpness of the edge is adjusted by the diffuseness parameter δ. This is the expression we will use to describe the low-energy stopping cross section as obtained by the END approach, that is, we adjust A, B, v_{tr}, and δ to the END *ab initio* numerical results.

B. High-energy stopping cross section

In the independent particle model [42], the electronic stopping cross section, within the first Born approximation, is written as

$$S_e^H(v) = \sum_i S_{e,i}(v), \tag{36}$$

where

$$S_{e,i} = \frac{4\pi e^4 Z_p^2}{m_e v^2} \int_{q_{\min}}^{q_{\max}} \frac{F_{n0}(q)}{q}\, dq \tag{37}$$

is the contribution of the ith electron, q goes from a minimum $q_{\min}$ to a maximum $q_{\max}$ momentum transfer, and $F_{n0}(q)$ are the generalized oscillator strengths (GOSs). When a target's electron is described under the assumption of being harmonically bound with an angular frequency ω_{0n}, the target's electronic spectrum is replaced by that of a harmonic oscillator (HO) [42]. One consequence of the HO model is that the orbital mean excitation energy is related to the orbital electron angular frequency as $I_{0i} = \hbar\omega_{0i}$, connecting directly the HO angular frequency ω_{0i} and the orbital mean excitation energy I_{0i}, i.e., $I_{0i} = \hbar\omega_{0i}$. The GOSs have already been determined for the HO and an analytical expression for the electronic stopping cross section, given in terms of the projectile and target properties, has been reported [28]. The simple expression for the orbital stopping cross section, valid at high collision velocities, is

$$S_{e,i}(v) = \frac{\pi e^4 Z_p^{*2}}{I_{0i}}\frac{\ln(1 + 16\epsilon^2)}{(c + \epsilon)}, \tag{38}$$

where ϵ is the reduced energy given by

$$\epsilon = \frac{m_e E_p}{M_p I_{0i}}. \tag{39}$$

Here, Z_p^* is the projectile effective charge and c takes the value of $2/\pi$ for the case of a harmonic oscillator [43].

We will use Eq. (36) together with Eq. (38) for the electronic stopping cross section at high collision energies. The values of the orbital mean excitation energy have been already reported by Cabrera-Trujillo [42] when replacing the HO spectrum by a self-consistent field (SCF) approach through the virial theorem in an atomic system.

C. Analytical expression for the electronic stopping cross section

Now, we are in position to match these two behaviors. As originally proposed by Montenegro *et al.* [15], we
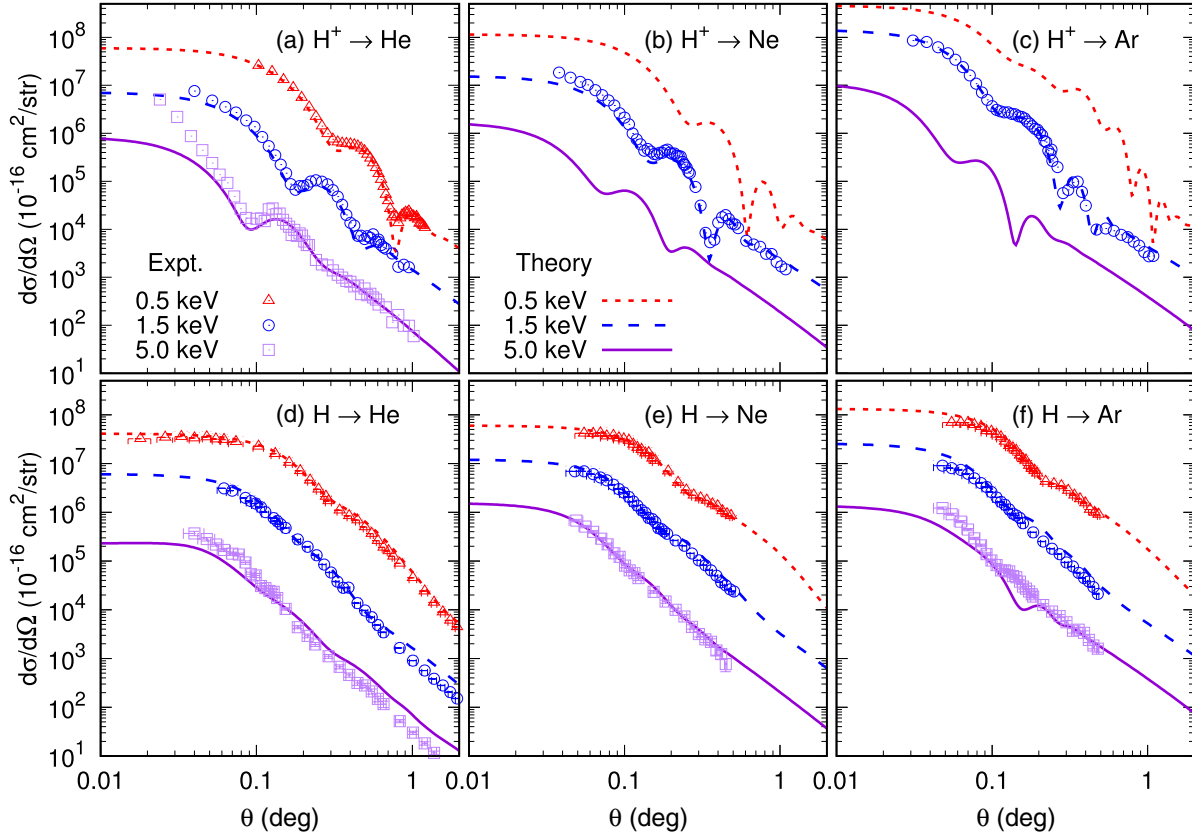
FIG. 1. Direct differential cross section for H$^+$ and H atoms incident in He, Ne, and Ar atoms for collision energies of 0.5, 1.5, and 5.0 keV/amu equivalent to a projectile velocity of 0.1415, 0.245, and 0.4475 a.u., as a function of the scattering angle in the laboratory frame. The experimental data are from the AMO group at Rice University. Specifically, for H$^+$ + He are from Johnson *et al.* [44], H + He, H + Ne, and H + Ar are from Gao *et al.* [45], and H$^+$ + Ne and H$^+$ + Ar are from Johnson *et al.* [46]. See text for discussion.

recognize the probabilistic character of the stopping cross section. Following the same line of reasoning, we assume that the probability for a proton to remain in a particular charge state, as a function of velocity, can be approximated analytically by

$$P \approx e^{-u}. \tag{40}$$

Thus, we postulate that the electronic stopping cross section is given by

$$S_e(v) = S_e^L(v)P + S_e^H(v)(1 - P), \tag{41}$$

which corresponds to a weighted electronic stopping cross section over the low- and high-energy regions. Consequently, our universal expression for the electronic stopping cross section is given by

$$S_e(v) = \left\{ Av + (B - A)\delta \ln \left[\frac{1 + e^{(v - v_{tr})/\delta}}{1 + e^{-v_{tr}/\delta}} \right] \right\} e^{-u}$$
$$+ (1 - e^{-u}) \sum_i \frac{\pi e^4 Z_p^{*2}}{I_{0i}} \frac{\ln(1 + 16\epsilon^2)}{(c + \epsilon)}, \tag{42}$$

where ϵ is given by Eq. (39). Thus, the only parameters that characterize the general expression for the electronic stopping cross section are A, B, δ, v_{tr}, I_{0i}, and c, all of them obtained from theoretical considerations. Note that at high collision energies we use $Z_p^* = Z_p$.

III. RESULTS AND DISCUSSION

A. Low-energy END results

1. Direct differential cross section

In Fig. 1, we show the direct differential cross section for H$^+$ and H projectiles when colliding with He, Ne, and Ar targets as a function of the laboratory scattering angle as obtained within the Schiff approximation, Eq. (5), from our END trajectories. The results are shown for collision energies of 0.5, 1.5, and 5 keV/amu equivalent to a projectile velocity of 0.1415, 0.245, and 0.4475 a.u. In Fig. 1(a), we show the results for H$^+$ colliding on He (lines) and we compare to the experimental data of Johnson *et al.* [44] showing an excellent agreement. Notice in particular the good description of the interference effects due to the rainbow and glory angles. This is a consequence of the proton penetrating the He electronic cloud and being repelled for small impact parameters and attracted for large impact parameters. In Fig. 1(d), we show the neutral case, H projectiles colliding with He, and we compare to the experimental data of Gao *et al.* [45], showing again a good to excellent agreement. In this case, the whole collision is repulsive, with no penetration of electronic clouds.

In Fig. 1(b), we show the case for a Ne target when a H$^+$ projectile collides with it. The experimental data are from Johnson *et al.* [46], showing again an excellent agreement to our theoretical results. The neutral case is shown in Fig. 1(e)
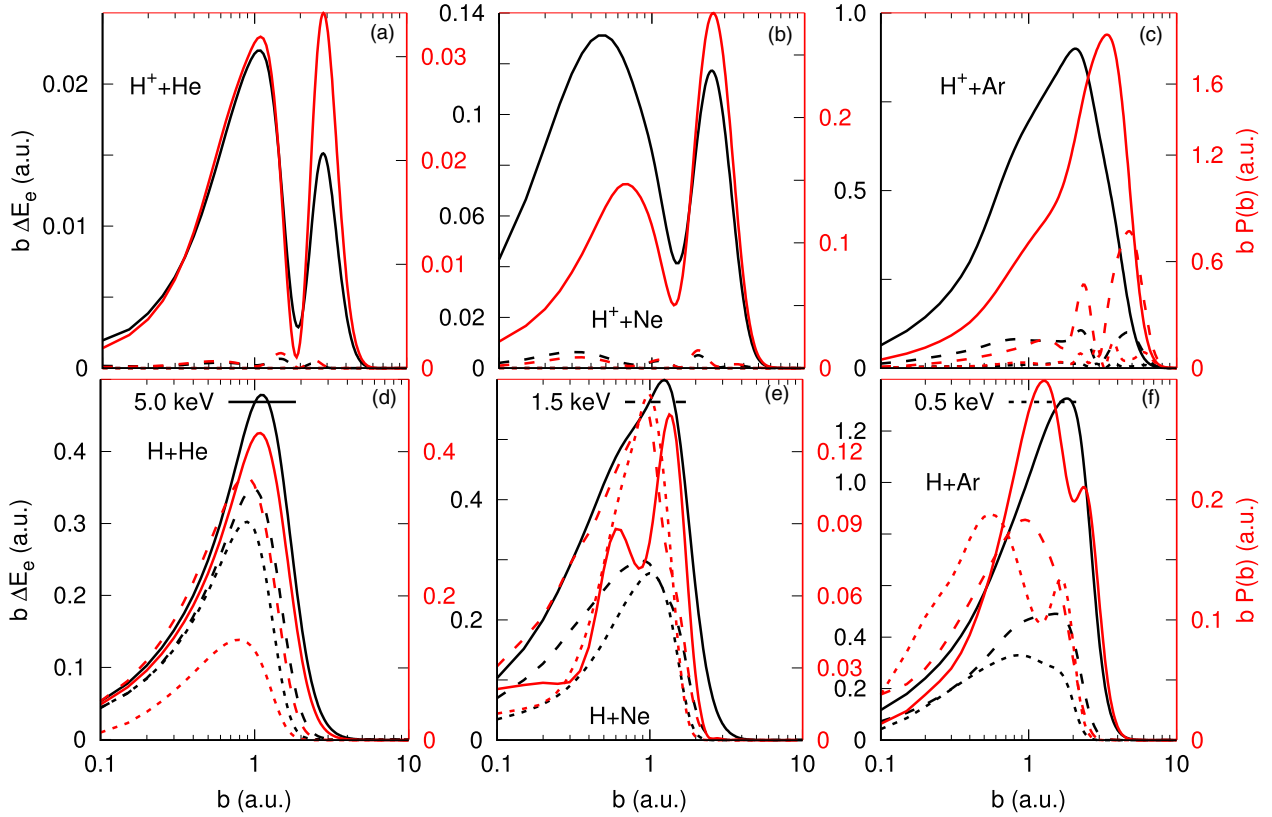
FIG. 2. Electronic energy loss (black lines) and charge-exchange probability (red lines) for H^+ and H atoms incident in He, Ne, and Ar atoms for collision energies of 0.5, 1.5, and 5.0 keV/amu equivalent to a projectile velocity of 0.1415, 0.245, and 0.4475 a.u., as a function of the impact parameter b. See text for discussion.

where neutral H collides with Ne and we compare to the experimental data of Gao *et al.* [45], showing an excellent agreement for all three collisions considered.

Finally, in Fig. 1(c), we show the case for a neutral Ar target when H^+ collides with it and we compare to the experimental data of Johnson *et al.* [46], showing excellent agreement and a good description of the scattering process. In Fig. 1(f), we show the case for neutral H colliding with Ar and its comparison to the experimental data of Gao *et al.* [45]. In this case, the collisions at 0.5 and 1.5 keV/amu show an excellent agreement. However, in the case for 5 keV/amu, we present a bump, which results from the interference effect present in the deflection function. This is a consequence of the slightly smaller basis set used to describe the hydrogen projectile as compared to the Ar target. Thus, our END results show a good to excellent agreement for H^+ and H when colliding with neutral He, Ne, and Ar showing a good description of the scattering process as a result of the correct trajectory description of the dynamics. Similar results are obtained for the other atomic gas targets considered in this work but are not shown.

2. Energy loss and charge exchange

In Fig. 2, we show the energy loss of the projectile transferred as excitations, weighted by the impact parameter for H^+ and H projectiles colliding with He, Ne, and Ar (black lines) as a function of the impact parameter for the collision

energies of 0.5, 1.5, and 5.0 keV/amu. In the same figure, we show the charge exchange probability on the projectile, weighted by the impact parameter (red lines). The case of H^+ colliding on He is shown in Fig. 2(a). Interestingly, we note that the energy loss has the same structure as the proton charge capture, except for the scale. This is observed for the three collision energies and for all the cases considered here, showing a correlation between the energy loss and the charge-transfer process. The same behavior is observed for the neutral case, shown in Fig. 2(d) for H colliding on He. In the case of H^+ colliding with Ne, we find that for intermediate impact parameters, $b > 1$, the energy-loss and charge-exchange process are correlated. The same is observed for the neutral cases of H colliding with Ne in Fig. 2(c), except for the scale. Finally, in Figs. 2(c) and 2(f) we show the case for H^+ and H colliding with Ar targets, respectively. A similar correlation between the energy-loss and charge-transfer process is observed in this case as a function of the impact parameter.

3. Beam charge fraction

With the integration of the charge-exchange probabilities, one determines the electron-capture cross section σ_{10} and the electron-loss cross section σ_{01} as required by Eqs. (23) and (24) to determine the charge fraction of the beam and the contributions from protons and neutral hydrogen projectiles as they interact with the target. In Fig. 3, we show the *ab initio* results, as obtained with END for the charge beam fraction of
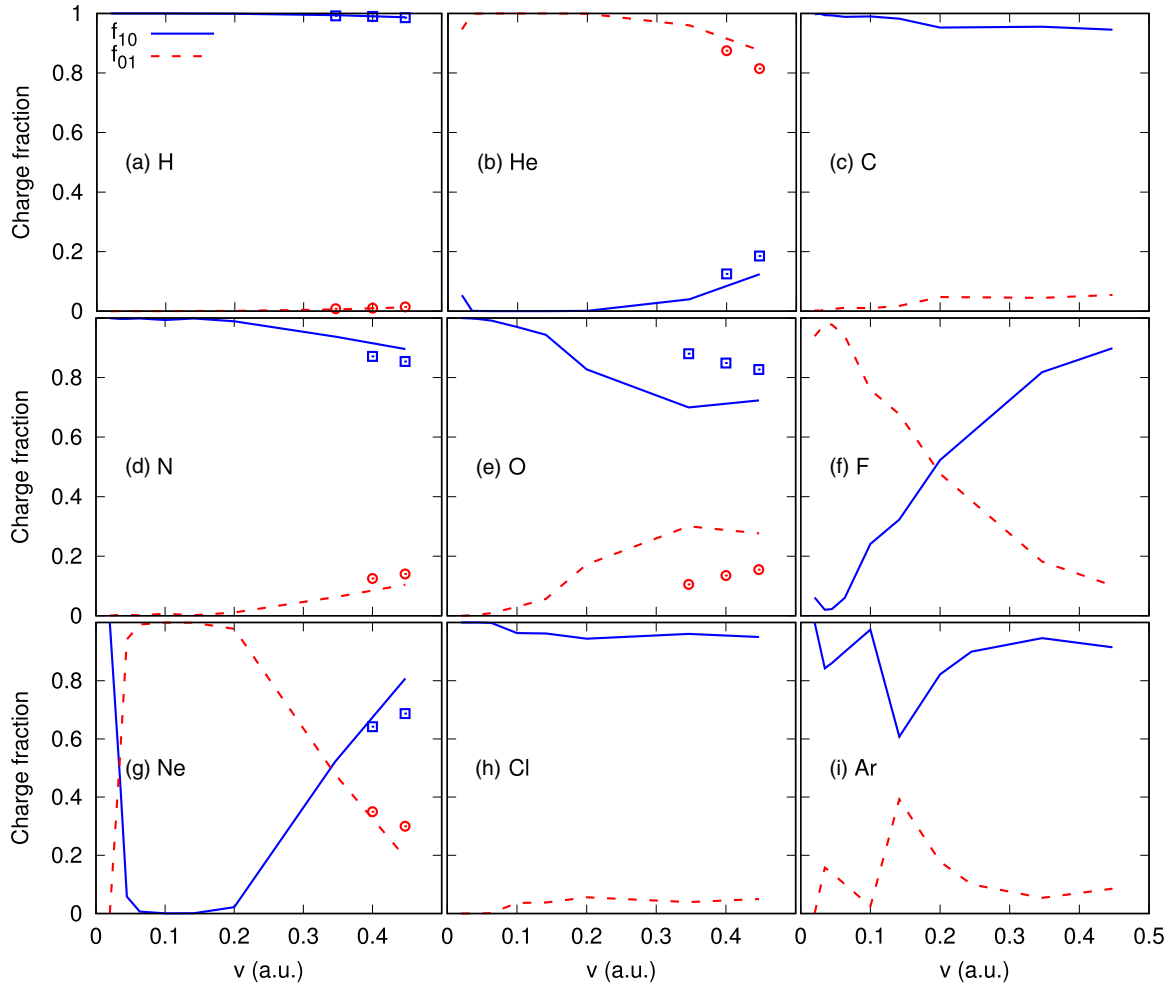
FIG. 3. Hydrogen beam charge fraction as a function of the projectile velocity, in the low collision energy region. The blue solid line corresponds to electron capture f_{10}, i.e., the hydrogen projectiles present in the beam, and the red dashed line corresponds to the electron loss f_{10}, i.e., the number of proton projectiles present in the beam. The symbols are the experimental data of Allison [47].

protons and hydrogen projectiles when colliding with the gas phase targets H, He, C, N, O, F, Ne, Cl, and Ar. The blue solid line corresponds to the neutral hydrogen beam fraction f_{10} while the red dashed line corresponds to the proton fraction in the beam f_{01}. In the same figure, we compare to the experimental data, as reported by Allison [47], showing a good to excellent agreement.

In Fig. 3(a), we show the results for a hydrogen beam colliding with atomic hydrogen. We find that the beam consists principally of neutralized hydrogen atoms as a consequence of the high electron capture of a proton when colliding with an atomic hydrogen target. The proton beam has a small fraction, which implies that the stopping cross section is dominated by the neutral hydrogen fraction. In Fig. 3(b), we show the charge fraction beam for a hydrogen beam colliding with a helium atom. In this case, the dominant fraction in the beam is the proton ion, due to the very small charge capture cross section of a proton when colliding with a helium atom. This behavior is a consequence of the high ionization potential of the helium target. In Figs. 3(c)–3(e), we show the results for a hydrogen beam colliding with atomic carbon, nitrogen, and oxygen gas phase targets, respectively. Our results for a

nitrogen target agree well with the experimental results of Allison [47]. However, the case of an oxygen target shows a difference of around 10% when compared to the Allison results. In both cases, the contribution of the proton beam charge fraction increases, with respect to the previous cases. A possible explanation for this behavior in our theoretical approach is the difficulty to treat the atomic oxygen atom within a single determinant as the one used by END. The case for a fluorine atomic target is shown in Fig. 3(f) where the high ionization potential of fluorine produces a large contribution from the proton at collision velocities below 0.2 a.u. while the neutral hydrogen beam starts to have a larger contribution for $v > 0.2$ a.u. The same occurs for a neon target, shown in Fig. 3(g) around $v \approx 0.32$ a.u., however, in this case we find an inversion at very low collision energies. A possible reason for this behavior is the fact that at low collision energies, the small electron-gain and -loss cross section starts to compete within these basis set descriptions due to its limited size. Finally, the cases of chlorine and argon are shown in Figs. 3(h) and 3(i), where the hydrogen atom fraction of the beam starts to dominate, as a consequence of a lower ionization potential as compared to helium and neon. Again, the behavior
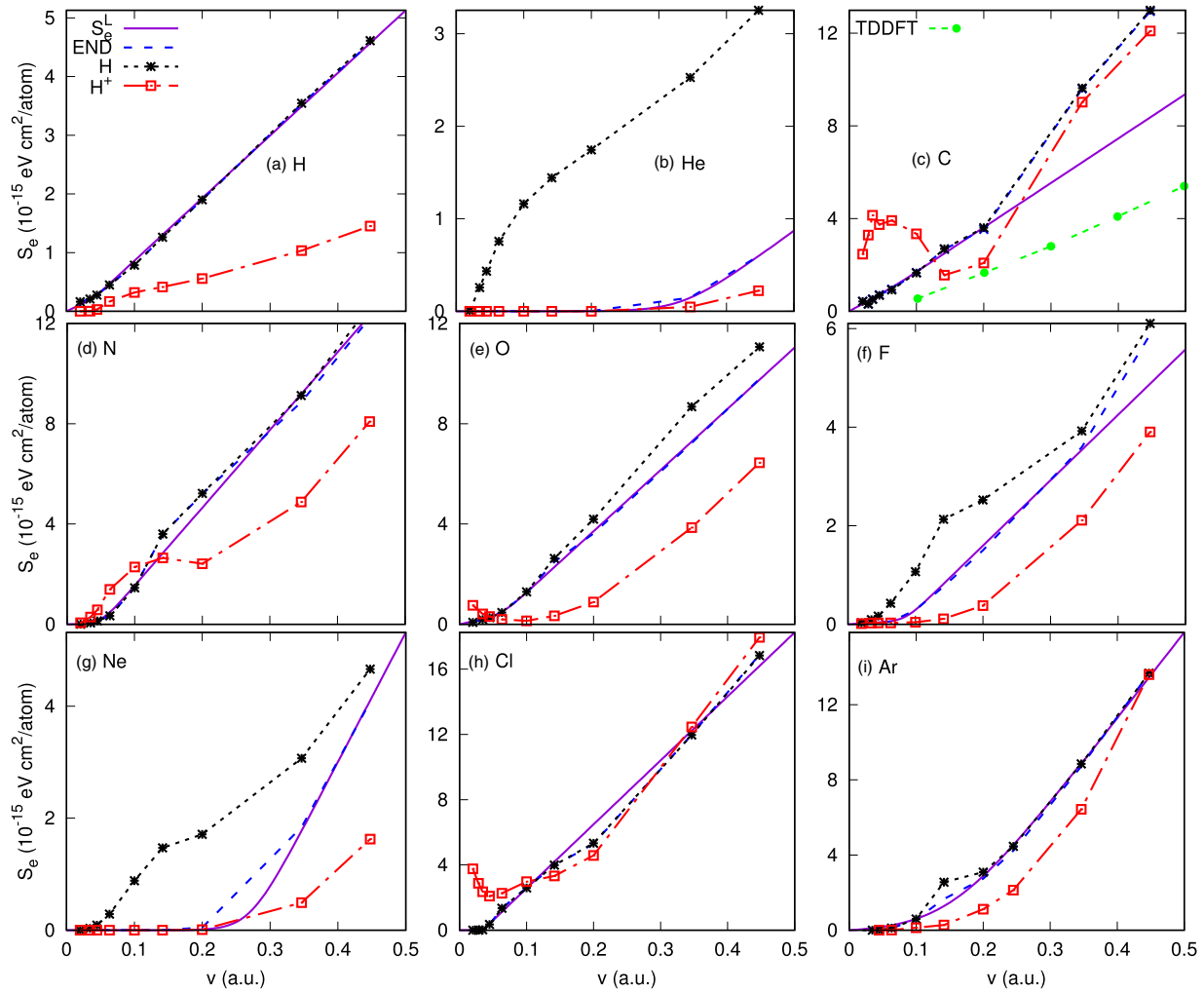
FIG. 4. Stopping cross section for hydrogen projectiles colliding on H, He, C, N, O, F, Ne, Cl, and Ar targets, as a function of the projectile velocities up to 0.45 a.u. (equivalent to 5 keV/amu collision energy). The black dashed line with a star symbol is the result for neutral hydrogen projectiles and the red dotted-dashed line with open square symbols is for protons as obtained with the END approach. The blue long-dashed line is the result of averaging through the charge beam contributions, Eq. (25). The purple solid line is the result of the bilinear Eq. (35) for S_e^L. The solid green circles with triple-dashed lines are the TDDFT results of Halliday and Artacho for hydrogen projectiles incident on graphite (carbon) [48] shown for comparison purposes. See text for discussion.

observed for the case of argon is a consequence the competition between electron gain and loss in the charge-transfer process within our basis sets.

4. Electronic stopping cross section

Now that we have the charge fractions in the beam and the energy loss of protons and hydrogen projectiles obtained with END at low collision energies, we proceed to study the electronic stopping cross section.

In Fig. 4, we show the electronic stopping cross section for hydrogen, helium, carbon, nitrogen, oxygen, fluorine, neon, chlorine, and argon gas targets for protons and hydrogen projectiles, as obtained by our *ab initio* END approach in the low velocity region. The red dotted-dashed line with open square symbols shows the END results at low collision energies for proton projectiles and the black short-dashed line with asterisk symbols is for neutral hydrogen projectiles' electronic stop-

ping cross section. The blue dashed line is the average over the charge fraction results from END and the purple solid line is the adjusted theoretical approach from Eq. (35) for S_e^L.

In Fig. 4(a), we find that for an atomic hydrogen target, both protons and neutral hydrogen produce an almost linear electronic stopping cross section. We also observe a slight threshold around 0.05 a.u. in the projectile velocity. The charge fraction analysis shows that because of the high electron charge transfer from the target to the projectile, the dominant beam charge is the neutral hydrogen projectile, i.e., the beam is neutralized. This produces a dominant electronic stopping cross section from neutral hydrogen beams, as expected. However, this is not the case for a helium target, as shown in Fig. 4(b). Here, as a consequence of the noble gas nature, it is very difficult to extract an electron from helium and consequently the dominant charge fraction in the beam is a proton beam for velocities up to 0.3 a.u. After that, high excitations start to become important. This is a consequence

of the high excitation gap in the helium atom as shown by the large threshold velocity, at $v_{tr} = 0.336$ a.u. The cases for carbon, nitrogen, and oxygen show a bilinear behavior in the electronic stopping cross section. For atomic carbon, in the gas phase, the open shell structure allows high excitations to become important at collision energies above 0.2 a.u. In a condensed phase, that would occur at higher collision energies due a larger energy gap introduced by the surrounding neighbors. In this case, the dominant channel is the neutral hydrogen beam. In nitrogen, we observe that both protons and hydrogen beams produce a similar stopping cross section, but the dominant beam charge fraction is the neutral hydrogen beam. This also occurs for oxygen. However, the ionization potential increases as the target nuclear number increases, such that the proton charge fraction increases. This makes the final S_e^L to depart from the neutral hydrogen contribution and increases the proton charge fraction contribution. However, the threshold is clearly discerned as well as the bilinear behavior. These projectile threshold energies are again of slightly higher consequence in the role of the polarization of the target electronic cloud. In all our results, we observe that our expression for the S_e^L adjusts correctly to the *ab initio* END averaged results from Eq. (25). In Fig. 4(f), we show the results for fluorine. In this case, for collision velocities above 0.3464 a.u., the electron capture dominates, but for lower collision energies it is the proton beam charge fraction that dominates, again as a consequence of the increase of the ionization potential. We observe a threshold effect that becomes more pronounced for the case of neon targets. The behavior of the Ne target, in Fig. 4(g), is very similar to the case of helium because as the target nuclear charge increases, so does the ionization potential, making it more difficult to exchange electrons to neutralize a proton beam and consequently the proton beam becomes more dominant. This has as a consequence an increasing threshold velocity, which is observed in the bilinear behavior of the electronic stopping cross section. However, the case of Ar does not follow this behavior. Here, the ionization potential is not as high as that of He or Ne and the neutral hydrogen beam is dominant, although at low collision we observe a threshold due to the large excitation gap.

In Table I, we provide the values for the low-energy stopping cross-section parameters, as required by Eq. (35) for reference purposes. The energy values for the orbital mean excitation energy have been already reported by the author in Ref. [42] and are used in the expression for the high-energy stopping cross section in Eq. (36). Notice that the values that c take are around 3, except for the He target where it is close to the theoretical value of the HO when a bare charged projectile collides. Except for H and O, we find thresholds ($A = 0$) in the electronic stopping cross section. The threshold velocity is between 50 and 100 eV, except for He and Ne where it is around 1–2 keV.

In Fig. 5, we show the results for the electronic stopping cross section from the low to high collision range, as obtained by the general expression, Eq. (42), for atomic hydrogen, helium, carbon, nitrogen, oxygen, fluorine, neon, chlorine, and argon targets in a gas phase for a hydrogen beam. The general expression is shown by a red dotted long-dashed line that goes from 10 eV/amu to 10 MeV/amu, that is a six

TABLE I. Parameters for the low-energy stopping cross-section expression, Eq. (35), as obtained with END. A and B are in 10^{-15} eV cm^2 when v is expressed in a.u. while δ and v_{tr} are in a.u. for velocity and c is dimensionless.

Target	A	B	δ	v_{tr}	c
H	5.5000	10.6723	0.0050	0.04000	2.47839
He	0.0000	5.3143	0.0316	0.33600	0.40018
C	16.0852	19.1826	0.0100	0.07000	4.50000
N	0.0000	30.9949	0.0100	0.05000	4.84400
O	5.8589	24.4211	0.0100	0.06328	3.74695
F	0.8000	13.2761	0.0100	0.08500	3.00000
Ne	0.0000	23.1153	0.0200	0.27000	3.61737
Cl	0.0000	39.2136	0.0020	0.03464	3.36259
Ar	0.0000	45.5856	0.0500	0.15000	3.13875

orders-of-magnitude range. The *ab initio* END results are shown by a blue dotted long-dashed line with a solid squared box in the low-energy region. In order to understand the behavior of the general expression, we also show its low- and high-energy contributions, S_e^L and S_e^H, respectively. The solid purple line is the low-energy contribution S_e^L, and the short-dashed black line is the high-energy contribution S_e^H. For comparison, we show Paul's IAEA experimental data compilation [49] with capital letter symbols as well as the empirical results from SRIM [21] shown by a brown long-dashed line. The experimental labels correspond to A [51], B [52], C [53], D [54], E [55], F [56], G [57], H [58], I [59], J [60], K [61], L [62], M [63], N [64], O [65], P [66], Q [67], R [68], S [69], T [70], U [71], V [72], W [73], X [74], Y [75], Z [76], and a [77]. Our expression completely agrees with the experimental data for atomic hydrogen targets, as shown in Fig. 5(a). Our END results predict a higher electronic energy loss, as a consequence of the gas phase state of the target, when compared to the SRIM data. Let us notice that the experimental data are obtained for molecular hydrogen targets while ours is for atomic targets. Note that our results predict a lower-energy loss at very low collision energies with a threshold energy around 60 eV/amu. This threshold projectile energy of 0.06 keV/amu is much lower than the predicted results from Eq. (29) for the first excitation energy of a hydrogen target of $\Delta E = 10.2$ eV. The predicted results of Eq. (29) are 2.34 keV/amu, which agrees completely well with the threshold observed for S_e^H (black dashed line) which is the expression that accounts for the direct excitations in the stopping cross section. The low S_e^L from END reports polarization effects induced by the collision interaction in the target electronic cloud. Interestingly, the low-energy contribution S_e^L extends to intermediate energies, as a consequence of the large charge exchange that neutralizes the beam. The high-energy contribution from protons becomes important at energies above 100 keV/amu.

In Fig. 5(b), we show the results for a helium target when a hydrogen beam impinges on it. Again, our results show an impressively good agreement with the experimental data compilation. Our results show a threshold energy around 3 keV/amu resulting from the large excitation gap in helium and the low charge-exchange process. This makes the low-energy
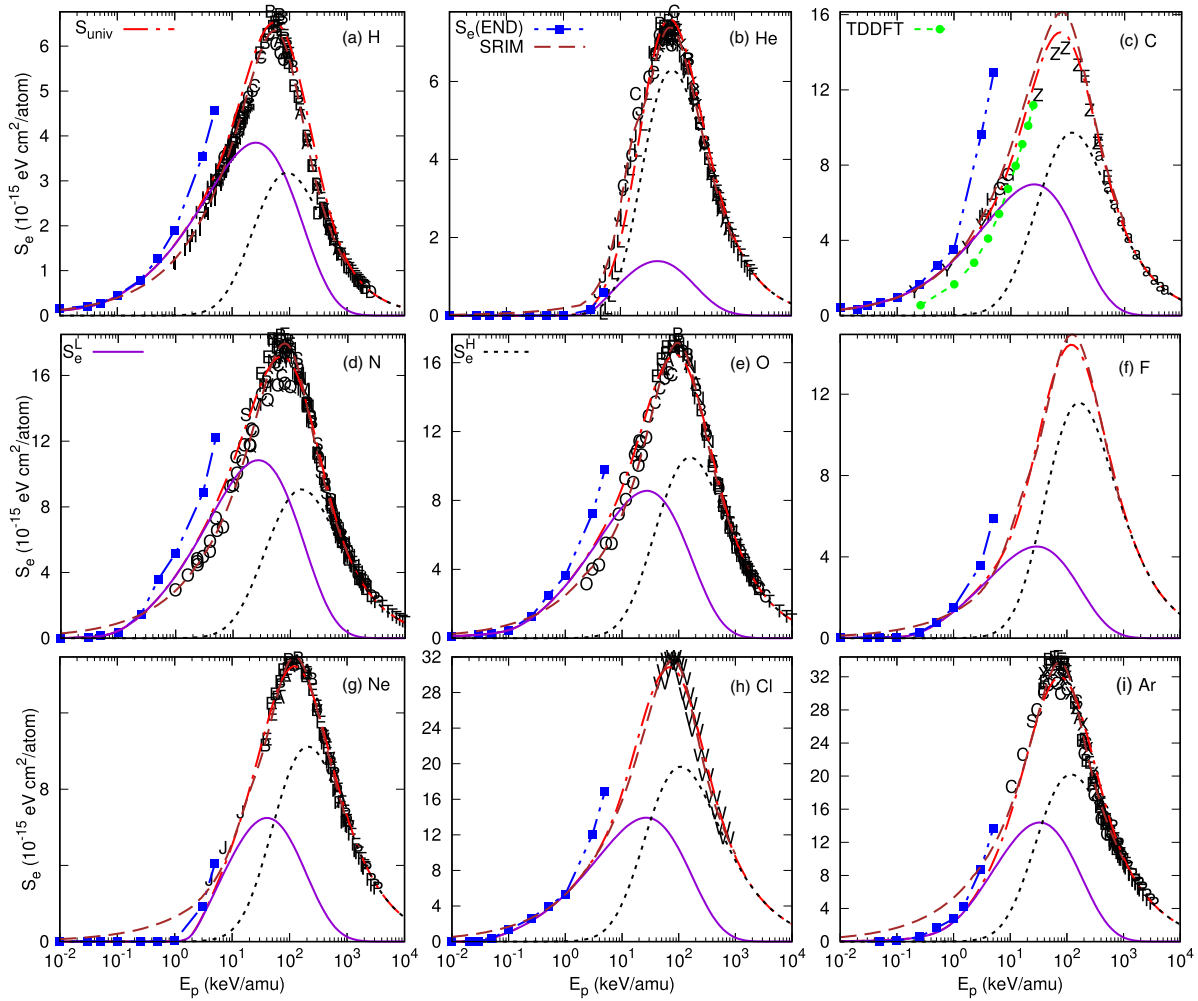
FIG. 5. Electronic and nuclear stopping cross sections for H, He, C, N, O, F, Ne, Cl, and Ar gas phase atoms for a hydrogen beam as a function of the collision energy. The red dotted long-dashed line is the result of the universal expression, Eq. (42). The *ab initio* END electronic stopping cross section is shown by blue dotted long-dashed line with a solid square symbol in the low-energy region. We also show the low- and high-energy contributions to the electronic stopping cross section by a purple solid line, S_e^L, and a dashed black line for S_e^H, respectively. For comparison, we show the results from SRIM [21] with a brown long-dashed line and also some experimental data, as compiled in Paul's database [49,50] shown with letter symbols. The experimental labels correspond to A [51], B [52], C [53], D [54], E [55], F [56], G [57], H [58], I [59], J [60], K [61], L [62], M [63], N [64], O [65], P [66], Q [67], R [68], S [69], T [70], U [71], V [72], W [73], X [74], Y [75], Z [76], and a [77]. In (c), the case for atomic carbon is compared the TDDFT results of Halliday and Artacho for hydrogen incident on graphite (carbon) [48] shown with solid green circles with triple-dashed lines for comparison purposes. See text for discussion.

contribution small and the high-energy contribution dominant, contrary to the hydrogen target case. This threshold energy agrees well with Eq. (29) for the first excitation of a helium atom of $\Delta E = 20.956$ eV as reported by the Atomic Spectra Database of NIST [78], such that we find a projectile threshold energy of 7.7 keV. Again, this agrees with the threshold observed for S_e^H for the direct excitations, as here the low-energy-loss contribution is small.

In Fig. 5(c), we show the case of a hydrogen beam colliding with atomic carbon (gas phase). This case is shown to prove the feasibility of our expression to be applied in condensed phase materials. Let us keep in mind that the parametrization of the bilinear expression has to be carried out through a theoretical approach that accounts for the condensed phase effects. However, we show that when using a gas phase approach such as END, we obtain excellent agreement when compared to the

available experimental data. The atomic gas phase description by END is shown in good agreement up to 1 keV. At higher collision energies, a better condensed phase description is required.

In Fig. 5(d), we show the results for a gas phase atomic nitrogen target when bombarded with a hydrogen beam. Notice that our expression predicts a large low-energy stopping cross-section contribution, similar to the hydrogen target behavior, with a very good comparison the experiment. When the charge-exchange process and energy loss is described properly by the *ab initio* END approach, then the universal expression has an excellent agreement with the experimental data, as observed for atomic oxygen targets, as shown in Fig. 5(e). As the ionization potential increases, the high-energy contribution increases too. Notice that the results for atomic oxygen are also in excellent agreement, despite the
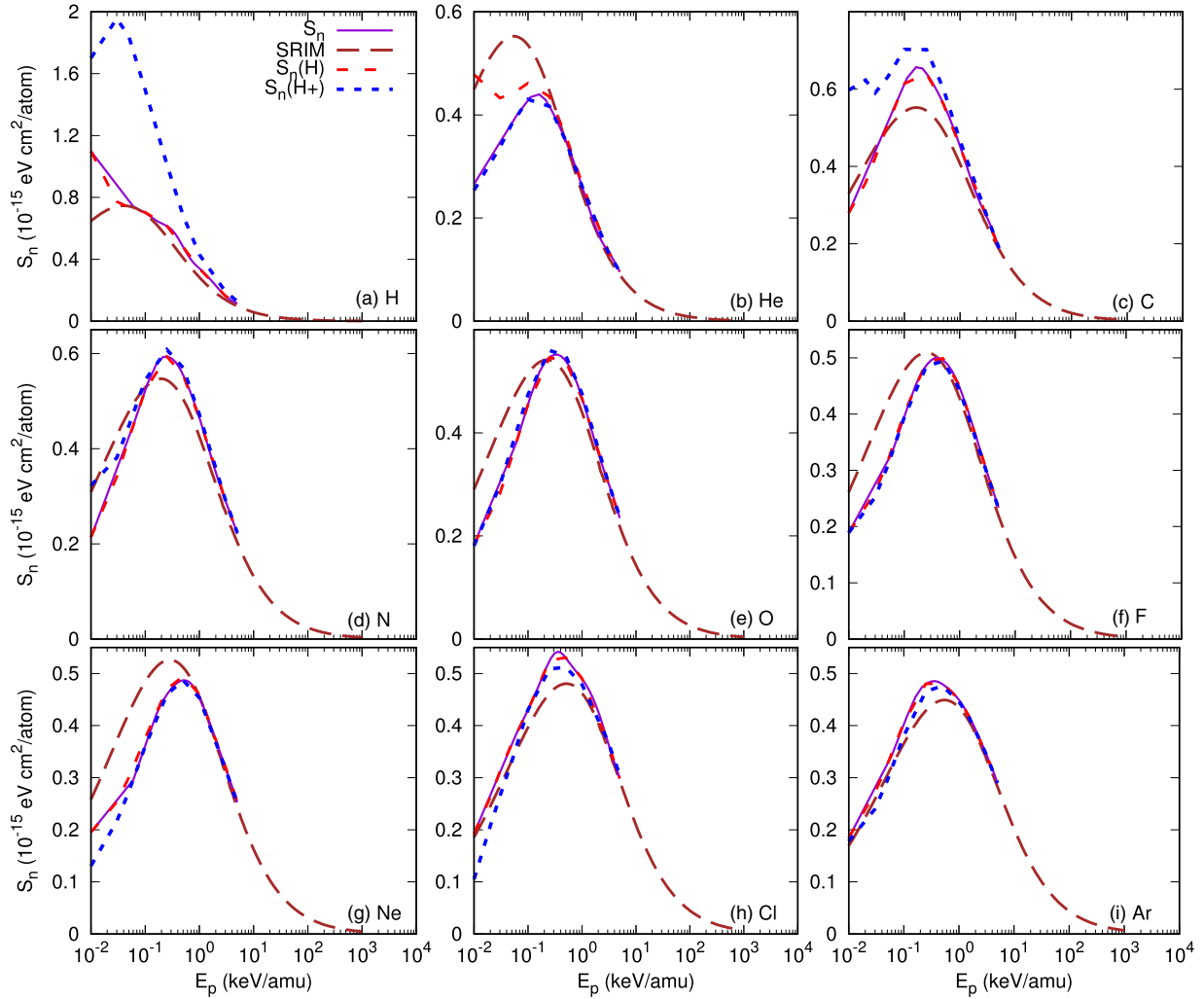
FIG. 6. Nuclear stopping cross section for H, He, C, N, O, F, Ne, Cl, and Ar gas phase atoms for a hydrogen beam as a function of the projectile collision energy. The red medium-dashed line is the result of Eq. (25). For comparison, we show the results from SRIM [21] with a brown long-dashed line. See text for discussion.

experimental data being for a molecular oxygen target. The difference is shown in the low-energy collision. In all our results, we can observe the bilinear behavior shown in Fig. 4 and the respective threshold effects as a consequence of the excitation gap as the ionization potential increases. In this case, Eq. (29) predicts a threshold velocity of 0.42 and 0.39 a.u. in the projectile velocity, corresponding to 4.4 and 3.9 keV/amu in the projectile energy, respectively, for the first excitation of $\Delta E = 10.3$ and 9.14 eV for N and O targets as reported by NIST [78]. The agreement with the threshold projectile energy observed in S_e^H is excellent.

In Figs. 5(f)–5(i), we show the results for the case of fluorine through argon gas phase atomic targets. There is no experimental data available for the case of a fluorine target, however, we find an excellent agreement with SRIM. Furthermore, our results show an impressively good agreement with the experimental data for the case of a neon target, as shown by Fig. 5(g). Here, the excitation threshold occurs at 1 keV/amu and our universal curve matches all the experimental data. For F and Ne, NIST reports $\Delta E = 12.7$ and 16.61 eV corresponding to 5.5 and 7.3 keV/amu, in agreement with the observed

threshold shown by S_e^H. The cases for chlorine and argon, shown in Figs. 5(h) and 5(i), are in excellent agreement with the available experimental data. Our results predict an increasing contribution from the high-energy region as the ionization potential increases as well as a threshold energy. In this case, the NIST ASD database reports $\Delta E = 8.92$ and 11.54 eV [78] for the first direct excitation of Cl and Ar with a corresponding threshold energy reported by Eq. (29) of 4 and 5.2 keV/amu and in excellent agreement with the high-energy stopping cross section S_e^H. Thus, we find that the threshold predicted by Eq. (29) corresponds to the high-energy expression S_e^H given by Eq. (36), while the results obtained by S_e^L correspond to the polarization (dragging or friction force) at low collision energy and in agreement with the experimental data.

5. Nuclear stopping cross section

In Fig. 6, we show the nuclear stopping cross section as obtained by the END approach for H$^+$ (blue short-dashed line) and neutral H (red medium-dashed line). In the same figure, we show the averaged result over the beam charge fraction

shown by the purple solid line. For comparison purposes, we show the nuclear stopping cross section as obtained by the SRIM approach (brown long-dashed line). In Fig. 6(a), we show the results for a hydrogen beam colliding with an atomic hydrogen gas target. We find that due to the same projectile-target mass, the projectile charge makes a large difference between the energy loss of protons and neutral hydrogen projectiles when interacting with atomic hydrogen. Due to the neutral hydrogen charge fraction in the beam, the dominant contribution is due to neutral hydrogen collisions, with a very good agreement with the SRIM results for $E > 100$ eV. For lower collision energies, we predict a larger nuclear energy loss. The case of a helium target is shown in Fig. 6(b). Here, the dominant beam charge fraction is the proton, with a similar contribution as the neutral hydrogen for collision energies above 200 eV and in excellent agreement with SRIM. For collision energies below 200 eV, we have a smaller nuclear stopping cross section than SRIM. In Fig. 6(c), we show the results for atomic carbon, while in Fig. 6(d), we show the results for atomic nitrogen, where we observe that both the hydrogen and proton energy loss is very similar and in good agreement with SRIM results, but with a smaller contribution from END for collision energies below 100 eV. The case of an oxygen target is shown in Fig. 6(e), where the proton and hydrogen beams have the same nuclear energy loss and with a very good agreement with SRIM for collision energies above 100 eV. This same behavior is observed for F, Ne, Cl, and Ar in Figs. 6(f)–6(i) where the proton and neutral hydrogen beams have similar energy losses. All these previous results have a good comparison with the results of SRIM. Let us recall that the SRIM results are obtained with a universal potential proposed by Andersen and Ziegler [20]. From our results, we confirm that this universal potential has a very good description of the nuclear energy loss for the case of heavy targets for collision energies above 100 eV/amu.

IV. CONCLUSIONS

We have derived a general expression for the electronic stopping cross section for a gas phase atomic target when a hydrogen beam slows down. Our expression is based on an *ab initio* approach to account for the electronic excitations and charge-exchange processes at low collision energies and the correct Bethe approach at high collision energies. Interestingly enough, the equation is simple and accurate. The universal expression has the proper limits at low and high collision energies and captures the threshold effects correctly. For the low collision energy, we use the electron-nuclear dynamics to obtain the correct description of the slowdown process as well as the electron-capture and scattering processes. With that, we report an analytic expression at low collision energy. By using a probabilistic approach, we match it to the Bethe electronic stopping cross section at high collision energies by means of the charge fraction of the beam. A systematic test of the equation against experiments shows a very good to excellent agreement, which strengthens the physical basis on which the equation has been derived. Of major relevance is that our low-energy stopping cross section is bilinear in the projectile velocity describing properly the threshold effects due to the excitation spectrum of the target. We find that the experimental threshold energy corresponds to dragging or friction effects in the low-energy region, while our previous reported theoretical result from Bethe's theory works in the high-energy contribution. We find that the charge-exchange process is crucial to describe properly the low-energy region up to the maximum of the stopping curve. At high energies, a general analytical expression based on the harmonic oscillator representation provides an excellent description of the excitation process when adapted to an atomic target.

Work is in progress to extend this approach to the whole periodic table as well as to molecular targets with the incorporation of phase effects.

[1] E. Rutherford, London, Edinburgh Dublin Philos. Mag. J. Sci. **21**, 669 (1911).

[2] A. V. Krasheninnikov, Y. Miyamoto, and D. Tománek, Phys. Rev. Lett. **99**, 016104 (2007).

[3] H. Bethe, Ann. Phys. **397**, 325 (1930).

[4] H. Bethe, Z. Phys. **76**, 293 (1932).

[5] R. Cabrera-Trujillo, Y. Ohrn, E. Deumens, and J. R. Sabin, J. Chem. Phys. **116**, 2783 (2002).

[6] N. Schlünzen, K. Balzer, M. Bonitz, L. Deuchler, and E. Pehlke, Contrib. Plasma Phys. **59**, e201800184 (2019).

[7] T. Kunert and R. Schmidt, Phys. Rev. Lett. **86**, 5258 (2001).

[8] N. Bohr, London, Edinburgh Dublin Philos. Mag. J. Sci. **25**, 10 (1913).

[9] N. Bohr, London, Edinburgh Dublin Philos. Mag. J. Sci. **30**, 581 (1915).

[10] E. Fermi and E. Teller, Phys. Rev. **72**, 399 (1947).

[11] J. Lindhard and M. Scharff, Kgl. Dan. Vidensk. Selsk. Mat. Fys. Medd. **27**, 1 (1953).

[12] O. Firsov, JETP **9**, 1076 (1959).

[13] A. F. Burenkov, F. F. Komarov, and M. M. Temkin, Radiat. Eff. **46**, 59 (1980).

[14] H. Sugiyama, Radiat. Eff. **56**, 205 (1981).

[15] E. Montenegro, S. Cruz, and C. Vargas-Aburto, Phys. Lett. A **92**, 195 (1982).

[16] Q. Wang and C. He, Radiat. Eff. Defects Solids **159**, 81 (2004).

[17] O. Kabadayi and H. Gümüs, Physica Status Solidi B **242**, 2391 (2005).

[18] H. Güumüs and O. Kabadayi, Vacuum **79**, 155 (2005).

[19] I. A. Akhiezer and L. N. Davydov, Sov. Phys. Usp. **22**, 804 (1979).

[20] H. Andersen and J. Ziegler, in *Stopping Powers and Ranges of Ions in Matter* (Pergamon Press, New York, 1977), p. 321.

[21] J. F. Ziegler, Nucl. Instrum. Methods Phys. Res. Sect. B **219-220**, 1027 (2004).

[22] G. Schiwietz, Phys. Rev. A **42**, 296 (1990).

[23] J. M. Pruneda, D. Sánchez-Portal, A. Arnau, J. I. Juaristi, and E. Artacho, Phys. Rev. Lett. **99**, 235501 (2007).

[24] R. Ullah, E. Artacho, and A. A. Correa, Phys. Rev. Lett. **121**, 116401 (2018).

[25] D. Roth, B. Bruckner, M. V. Moro, S. Gruber, D. Goebl, J. I. Juaristi, M. Alducin, R. Steinberger, J. Duchoslav, D. Primetzhofer, and P. Bauer, Phys. Rev. Lett. **118**, 103401 (2017).

[26] D. Roth, B. Bruckner, G. Undeutsch, V. Paneta, A. I. Mardare, C. L. McGahan, M. Dosmailov, J. I. Juaristi, M. Alducin, J. D. Pedarnig, R. F. Haglund, D. Primetzhofer, and P. Bauer, Phys. Rev. Lett. **119**, 163401 (2017).

[27] E. Deumens, A. Diz, R. Longo, and Y. Öhrn, Rev. Mod. Phys. **66**, 917 (1994).

[28] L. Trujillo-Lopez and R. Cabrera-Trujillo, Radiat. Phys. Chem. **156**, 150 (2019).

[29] L. I. Schiff, Phys. Rev. **103**, 443 (1956).

[30] R. Cabrera-Trujillo, J. R. Sabin, Y. Öhrn, and E. Deumens, Phys. Rev. A **61**, 032719 (2000).

[31] R. Cabrera-Trujillo, J. Sabin, E. Deumens, and Y. Ohrn, in *Theory of the Interaction of Swift Ions with Matter. Part 1*, Advances in Quantum Chemistry Vol. 45 (Academic Press, New York, 2004), pp. 99–124.

[32] D. Thouless, Nucl. Phys. **21**, 225 (1960).

[33] J. Klauder and B. Skagerstam, *Coherent States: Applications in Physics and Mathematical Physics* (World Scientific, Singapore, 1985).

[34] R. Cabrera-Trujillo, E. Deumens, Y. Ohrn, and J. R. Sabin, Nucl. Instrum. Methods Phys. Res. Sect. B **168**, 484 (2000).

[35] T. H. Dunning, J. Chem. Phys. **90**, 1007 (1989).

[36] N. Bohr, Mat. Fys. Medd. Dan. Vid. Selsk. **18**, No. 8 (1948).

[37] R. Cabrera-Trujillo, H. Bruhns, and D. W. Savin, Phys. Rev. A **101**, 052708 (2020).

[38] R. Cabrera-Trujillo, J. R. Sabin, Y. Öhrn, and E. Deumens, Phys. Rev. Lett. **84**, 5300 (2000).

[39] A. Dalgarno, G. W. Griffing, and D. R. Bates, Proc. R. Soc. London, Ser. A **232**, 423 (1955).

[40] M. Inokuti, Rev. Mod. Phys. **43**, 297 (1971).

[41] R. D. Woods and D. S. Saxon, Phys. Rev. **95**, 577 (1954).

[42] R. Cabrera-Trujillo, Phys. Rev. A **60**, 3044 (1999).

[43] R. Cabrera-Trujillo, C. Martinez-Flores, L. Trujillo-Lopez, and L. Serkovic-Loli, Radiat. Eff. Defects Solids **171**, 146 (2016).

[44] L. K. Johnson, R. S. Gao, R. G. Dixson, K. A. Smith, N. F. Lane, R. F. Stebbings, and M. Kimura, Phys. Rev. A **40**, 3626 (1989).

[45] R. S. Gao, L. K. Johnson, K. A. Smith, and R. F. Stebbings, Phys. Rev. A **40**, 4914 (1989).

[46] L. K. Johnson, R. S. Gao, C. L. Hakes, K. A. Smith, and R. F. Stebbings, Phys. Rev. A **40**, 4920 (1989).

[47] S. K. Allison, Rev. Mod. Phys. **30**, 1137 (1958).

[48] J. Halliday and E. Artacho, Phys. Rev. B **100**, 104112 (2019).

[49] IAEA electronic stopping power of matter for ions: Graphs, data, comments, and programs, https://www-nds.iaea.org/stopping, accessed 10 August 2020.

[50] C. Montanari and P. Dimitriou, Nucl. Instrum. Methods Phys. Res. Sect. B **408**, 50 (2017).

[51] H. Baumgart, W. Arnold, H. Berg, E. Huttel, and G. Clausnitzer, Nucl. Instrum. Methods Phys. Res. **204**, 597 (1983).

[52] F. Besenbacher, H. H. Andersen, P. Hvelplund, and H. Knudsen, Mat. Fys. Medd. K. Dan. Vidensk. Selsk. **40**, No. 3 (1979).

[53] J. A. Phillips, Phys. Rev. **90**, 532 (1953).

[54] R. A. Langley, Phys. Rev. B **12**, 3575 (1975).

[55] H. K. Reynolds, D. N. F. Dunbar, W. A. Wenzel, and W. Whaling, Phys. Rev. **92**, 742 (1953).

[56] G. Reiter, N. Kniest, E. Pfaff, and G. Clausnitzer, Nucl. Instrum. Methods Phys. Res. Sect. B **44**, 399 (1990).

[57] R. Golser, C. Eppacher, and D. Semrad, Nucl. Instrum. Methods Phys. Res. Sect. B **67**, 69 (1992).

[58] R. Golser and D. Semrad, Nucl. Instrum. Methods Phys. Res. Sect. B **69**, 18 (1992).

[59] P. Børgesen and H. Sørensen, Nucl. Instrum. Methods Phys. Res. **200**, 571 (1982).

[60] A. Schiefermüller, R. Golser, R. Stohl, and D. Semrad, Phys. Rev. A **48**, 4467 (1993).

[61] J. T. Park and E. J. Zimmerman, Phys. Rev. **131**, 1611 (1963).

[62] F. Raiola, G. Gyürky, M.Aliotta, A. Formicola, R. Bonetti, C. Broggini, L. Campajola, P. Corvisiero, H. Costantini, A. D'Onofrio, Z. Fülöp, G. Gervino, L. Gialanella, A. Guglielmetti, C. Gustavino, G. Imbriani, M. Junker, R. Kavanagh, P. Moroni, A. Ordine *et al.*, Eur. Phys. J. A **10**, 487 (2001).

[63] A. Fukuda, Phys. Med. Biol. **25**, 877 (1980).

[64] G. Reiter, H. Baumgart, N. Kniest, E. Pfaff, and G. Clausnitzer, Nucl. Instrum. Methods Phys. Res. Sect. B **27**, 287 (1987).

[65] V. Dose and G. Sele, Z. Phys. A **272**, 237 (1975).

[66] J. Swint, R. Prior, and J. Ramirez, Nucl. Instrum. Methods **80**, 134 (1970).

[67] J. H. Ormrod, Can. J. Phys. **46**, 497 (1968).

[68] A. B. Chilton, J. N. Cooper, and J. C. Harris, Phys. Rev. **93**, 413 (1954).

[69] R. L. Wolke, W. N. Bishop, E. Eichler, N. R. Johnson, and G. D. O'Kelley, Phys. Rev. **129**, 2591 (1963).

[70] N. Shiomi-Tsuda, N. Sakamoto, H. Ogawa, M. Tanaka, M. Saitoh, and U. Kitoba, Nucl. Instrum. Methods Phys. Res. Sect. B **149**, 17 (1999).

[71] P. Børgensen, C. Hao-Ming, and H. Sørensen, Nucl. Instrum. Methods Phys. Res. **194**, 71 (1982).

[72] E. Bonderup and P. Hvelplund, Phys. Rev. A **4**, 562 (1971).

[73] H. Baumgart, H. Berg, E. Huttel, E. Pfaff, G. Reiter, and G. Clausnitzer, Nucl. Instrum. Methods Phys. Res. Sect. B **2**, 145 (1984).

[74] P. K. Weyl, Phys. Rev. **91**, 289 (1953).

[75] S. H. Overbury, P. F. Dittner, S. Datz, and R. S. Thoe, Radiat. Eff. **41**, 219 (1979).

[76] P. Bauer, Nucl. Instrum. Methods Phys. Res. Sect. B **45**, 673 (1990).

[77] S. Gorodetzky, A. Chevallier, A. Pape, J. Sens, A. Bergdolt, M. Bres, and R. Armbruster, Nucl. Phys. A **91**, 133 (1967).

[78] A. Kramida, Yu. Ralchenko, J. Reader, and NIST ASD Team, NIST Atomic Spectra Database (ver. 5.8), https://physics.nist.gov/asd, National Institute of Standards and Technology, Gaithersburg, MD, accessed 26 December 2020.